VOL. 4, NO. 4, OCTOBER 1990 J. THERMOPHYSICS 485

Analytical Investigation of the Thermal Response of Decomposing Polymer Composites

John Florio Jr.*
Kaman Sciences Corporation, Burlington, Massachusetts
and
Jack B. Henderson†
University of Rhode Island, Kingston, Rhode Island

A numerical study of the thermally induced response of two widely used glass-filled polymer composites has been performed. This study was conducted using a newly developed mathematical model, which, unlike previous models, does not include the idealized assumption of local thermal equilibrium existing between the solid matrix and product gas. Experimentally determined volumetric heat transfer coefficients were used to characterize the rate of energy transfer between the two phases within the tortuous pore network of each material. These coefficients were introduced into the model in the form of a Nusselt number/Reynolds number correlation developed in this study. The results of the present investigation include solid temperature, product gas temperature, pyrolysis mass loss, pressure, gas mass flux, gas-storage ratio, and expansion and volumetric heat-transfer coefficient profiles. Material composition and processing were used to compare and contrast these results. Of particular interest, the deviation from thermal equilibrium in one material has been predicted to be as high as 500°C. A general discussion on the effect of the assumption of local thermal equilibrium is presented based on preliminary findings.

Nomenclature

a = Nusselt-Reynolds correlation coefficient
A = pre-exponential factor
b = Nusselt-Reynolds correlation coefficient, Eq. (13)
C_p = specific heat
E = activation energy
F = mass fraction of virgin material
h_v = volumetric heat transfer coefficient
H = specific enthalpy
k = thermal conductivity
L = specimen thickness
m = mass
$\dot{m}''$ = mass flux
M = molecular weight of gases
n = order reaction
P = pressure
Q = heat of decomposition
R = universal gas constant
t = time coordinate
U = specific internal energy
T = temperature
v = gas velocity
x = spatial coordinate
α = linear coefficient of thermal expansion
β = inertial coefficient
γ = permeability
δ = decomposition porosity coefficient
ΔA = cross-sectional area
Δx = control system width
ϵ = emissivity
ζ = decomposition permeability coefficient
η = heating-rate expansion coefficient
λ = generic variable
μ = viscosity
ξ = decomposition expansion coefficient
ρ = density
ϕ = porosity
Ψ = coefficient of linear permeability

Subscripts

c = char
f = final
g = gas
o = initial
s = solid
v = virgin

Introduction

OVER the past decade, polymer composite materials have become accepted in a wide variety of thermal-protection applications. Examples of these include spacecraft heat shields for re-entry, rocket motor nozzle liners, missile magazines, blast deflectors, etc. In the majority of these applications, the materials are exposed to temperatures high enough to cause decomposition of the solid material. In fact, overwhelming acceptance of these materials stems from a high char yield resulting from pyrolysis reactions, coupled with favorable thermal and transport properties of the product char. As a result of the decomposition process, the overall thermally induced behavior of the material is quite complex and varies with material composition and/or processing. In order to design these types of thermal-protection systems efficiently, it is necessary to predict accurately the overall response of these materials a priori.

The purpose of this work was to study the thermally induced response of glass-filled polymers using a newly developed, one-dimensional transient numerical model, which does not include the idealized assumption of local thermal equilibrium. Since the thermal response of these materials is highly transient, it is thought that large deviations from local thermal equilibrium do indeed exist. Clearly, the thermal decomposition of a composite material is enhanced with increased departure from thermal equilibrium. This implies that accurate modeling must include equations for energy conservation in both the solid and gas phases, coupled by the volumetric

---

Received June 8, 1989; revision received Oct. 6, 1989. Copyright © 1990 by the American Institute of Aeronautics and Astronautics, Inc. All rights reserved.

*Research Engineer, AviDyne Division.

†Professor, Department of Mechanical Engineering and Applied Mechanics.

heat-transfer coefficient. Although many excellent mathematical models exist in the open literature for the prediction of the thermal response of these and other materials,[1-5] to the best of the authors' knowledge there have been no in-depth analytical investigations dealing with the prediction of their overall response in the absence of local thermal equilibrium. The modeling technique in the present study also includes thermochemical expansion of the material and related work terms incorporated into the energy equations, which have not been included in many of the previous works. Lastly, aerospace companies have conducted numerous modeling studies in this area, the majority of which are classified and/or under limited distribution. For the most part, these studies incorporate the same simplifying assumptions as those in the open literature.

Material Behavior

When a polymer composite material is exposed to a surface heat flux, the initial heat transfer is primarily due to transient energy conduction. This heat condition is solely governed by the thermal properties of the virgin material. When the material reaches sufficiently high temperatures (200–300°C), dependent on material processing, composition, and heating rate, chemical reactions begin to occur. These thermally induced reactions, commonly referred to as pyrolysis reactions, result in the degradation of the resin component of the composite matrix to residue char and product volatiles. This reaction zone moves from the heated surface through the material. During the initial stages of the pyrolysis reactions, decomposition gases are trapped within the pore network due to low material permeability. This accumulation of gases results in the internal pressurization of the material. The internal pressurization is at least partially responsible for a very rapid and sometimes quite large expansion of the material that occurs at this time. As a result of the continuing expansion and decomposition, the material permeability and porosity begin to increase. This increased permeability, coupled with existing pressure gradients, results in the flow of gas through the pore network. As a result, energy is transferred between the product gas and solid material within the pore network by means of forced convection. This highly transient energy transfer results in large deviations from thermal equilibrium existing locally between the two phases. The gases that flow back through the char structure remove energy by convection with the solid, thus attentuating the conduction of heat to the reaction zone. The gases that flow in the other direction, through the partially virgin material, serve to preheat the material. The rate of doing work resulting from the flow of gas now becomes an important means of energy transfer. As the pryrolysis reactions and expansion proceed, the permeability and porosity of the material increase still further. This results in increased gas flow and in a reduction in internal pressure. When this occurs, the material experiences a rapid contraction, primarily due to elastic recovery.

At temperatures in excess of 1000° C, the carbonaceous char reacts with silica, present in the glass fibers, resulting in considerable additional mass loss. Given sufficient incident energy, the active material may entirely be consumed. The final products may include a combination of solid-phase silicon carbide and product gases or an entirely gaseous phase. The thermodynamic equilibrium distribution of products for this system (C-SiO_2), as a function of temperature, pressure, and substrate concentration, has been discussed by Ladacki.[6]

Model Description

A one-dimensional transient mathematical model has been developed to predict the thermally induced response of a polymer composite matrix in the absence of thermal equilibrium. Since heat transfer is accompanied by fluid flow, it was necessary to require the conservation of thermal energy, momentum, and mass in the system. Additionally, thermochemical expansion, solid matrix decomposition, and temperature-dependent property relations were included in the overall modeling scheme. The major simplifying assumptions incorporated into the model were that decomposition gases behave ideally and are inert, and that the specific internal energy of the solid is equivalent to the specific enthalpy of the solid.

The introduction of convective thermal transport between the solid and volatiles requires that separate energy equations be derived for each phase. An energy balance was applied over a nonstationary volume element, $\Delta A \Delta x$, to obtain the equations of energy for both the solid and gas phase. The following equations constitute the mathematical description for energy conservation in the overall model.

Solid:

$$\frac{\partial}{\partial t}(m_s U_s) = \Delta A\,\Delta x \frac{\partial}{\partial x}\left[k_s(1-\phi)\frac{\partial T_s}{\partial x}\right] + h_v \Delta A \Delta x (T_g - T_s) + P\phi\Delta A \frac{\partial \Delta x}{\partial t} - Q\frac{\partial m_s}{\partial t} + H_g(T_s)\frac{\partial m_s}{\partial t} \tag{1}$$

Gas:

$$\frac{\partial}{\partial t}\left[\left(\rho_g U_g + \frac{1}{2}\rho_g v^2\right)\Delta A\,\Delta x \phi\right] = \Delta A\,\Delta x \frac{\partial}{\partial x}\left(k_g \phi \frac{\partial T_g}{\partial x}\right) - \Delta A\,\Delta x \frac{\partial}{\partial x}\left[\left(\rho_g U_g + \frac{1}{2}\rho_g v^2\right)\phi v\right] + h_v \Delta A\,\Delta x (T_s - T_g) - P\phi\Delta A \frac{\partial \Delta x}{\partial t} - \Delta A \Delta x \frac{\partial (P\phi v)}{\partial x} - H_g(T_s)\frac{\partial m_s}{\partial t} \tag{2}$$

Equation (1) describes the transport of energy within the solid phase. The first term represents the accumulation of internal energy within the control system $\Delta A\,\Delta x$; the second term represents the net rate of energy transfer by condition; the third term represents the rate of energy transferred by convection between the solid material and volatiles; the fourth term accounts for the rate of work of expansion; the fifth term depicts energy consumption/generation during chemical reactions; and, finally, the last term accounts for the energy lost by the flow of newly generated product gas from the solid matrix into the gas stream, i.e., pore network. Radiation energy transfer within the pore network of the material has been neglected since simplified calculations show it to be smaller than energy transfer by means of conduction. This ideology was adopted by previous researchers.[1-5]

Equation (2) describes the transport of energy within the gas phase. The first term in this equation represents the accumulation of internal and kinetic energy; the second term represents the net rate of energy transfer by conduction; the third term represents the net rate of convection of internal and kinetic energy; the sixth term depicts the rate of doing work against the static pressure P at the control system faces, i.e., flow work.

The appropriate form of the equation of continuity was obtained by writing a mass balance over the nonstationary volume element, resulting in the following:

$$\frac{\partial m_g}{\partial t} = \frac{\partial m_s}{\partial t} - \Delta A\,\Delta x \frac{\partial \dot{m}''_g}{\partial x} \tag{3}$$

Momentum conservation is modeled using a non-Darcy type correlation, governing flow through porous media where $\beta = c\sqrt{\gamma}$; that is,

$$-\frac{\partial P}{\partial x} = \frac{\mu_g}{\rho_g \gamma}\dot{m}''_g + \frac{\beta \dot{m}''_g}{\rho_g}\,|\dot{m}''_g| \tag{4}$$

The rate of solid mass decomposition is calculated by an nth-order kinetic rate equation of the form

$$\frac{1}{m_o}\frac{\partial m_s}{\partial t} = -A\frac{(m_s - m_o)^n}{m_f}e^{[-E/RT_s]} \tag{5}$$

The thermochemical expansion of the control system Δx is modeled by an equation similar to that used by Henderson and Wiecek[5]:

$$\frac{1}{\Delta x}\frac{\partial \Delta x}{\partial t} = \alpha_v F\frac{\partial T_s}{\partial t} + \alpha_c\,(1-F)\frac{\partial T_s}{\partial t} + \frac{\partial}{\partial t}\left(\eta T_s + \xi\,\frac{m_s}{m_o}\right) \tag{6}$$

The permeability and porosity are given, respectively, as follows:

$$\frac{1}{\gamma_o}\frac{\partial \gamma}{\partial t} = \Psi_v F\frac{\partial T_s}{\partial t} + \Psi_c(1-F)\frac{\partial T_s}{\partial t} + \frac{\zeta}{m_o}\frac{\partial m_s}{\partial t} \tag{7}$$

and

$$\frac{1}{\phi_o}\frac{\partial \phi}{\partial t} = \frac{\delta}{m_o}\frac{\partial m_s}{\partial t} \tag{8}$$

The ideal-gas equation of state is used to specify the following relationship between the variables of state; i.e.,

$$P = \frac{m_g R T_g}{M\phi\Delta A\,\Delta x} \tag{9}$$

Lastly, the solid thermal conductivity, specific heat, and surface emissivity were determined by a weighted average of virgin and char material. That is,

$$\lambda = \lambda_v F + (1-F)\,\lambda_c \tag{10}$$

The final form of the solid thermal energy equation used in the numerical scheme was obtained by substituting the approximation $H_s = U_s$ into Eq. (1). This yields

$$m_s C_{p_s}\frac{\partial T_s}{\partial t} = \Delta A\,\Delta x\frac{\partial}{\partial x}\left[k_s(1-\phi)\frac{\partial T_s}{\partial x}\right] + h_v\Delta A\,\Delta x(T_g - T_s) + P\phi\Delta A\,\frac{\partial \Delta x}{\partial t} - \frac{\partial m_s}{\partial t}\left[H_s - H_g(T_s) + Q\right] \tag{11}$$

The final form of the gas thermal energy equation used in the numerical scheme was obtained by substituting the appropriate form of the mechanical energy equation into Eq. (2), and then introducing Eq. (3) into the resulting expression. This yields

$$m_g C_{p_g}\frac{\partial T_g}{\partial t} = \dot m_g''\,\Delta A\,\Delta x C_{p_g}\frac{\partial T_g}{\partial x} + \Delta A\,\Delta x\,\frac{\partial}{\partial x}\left(k_g\phi\,\frac{\partial T_g}{\partial x}\right) + h_v\Delta A\,\Delta x(T_s - T_g) + \Delta A\,\Delta x\,\frac{\mathrm{D}(\phi P)}{\mathrm{D}t} - \frac{\partial m_s}{\partial t}\,[-H_g + H_g(T_s) + v^2/2] \tag{12}$$

The volumetric heat transfer coefficient h_v is calculated based on the following correlation[7]:

$$Nu = aRe \tag{13}$$

where

$$Nu = \frac{h_v\gamma}{k_g} \tag{14}$$

$$Re = -\frac{\rho_g\gamma^{1.5}}{\mu_g^2\phi}\frac{\partial P}{\partial x} \tag{15}$$

Equations (11), (12), and (3-8) represent a set of coupled, nonlinear partial differential equations in T_s, T_g, $\dot m_g''$, P, m_s, Δx, γ, and ϕ, respectively. In the numerical scheme, this set of governing equations was approximated using a fully implicit finite-difference technique.

Materials

The two composites studied are designated as H41N and MXBE-350 and are fabricated by Ametek Haveg Division and Fiberite Corporation, respectively. These resins are of the thermosetting variety. Table 1 lists the constituents found in these materials. Both materials consist of a basic phenol-formaldehyde resin with varying quantities of fillers and reinforcing agents. These materials were chosen for study because they exhibit typical decomposition/length change behavior for glass-filled thermoset composites. Both materials are also of great practical importance since they are used extensively in high-temperature, high-heating-rate thermal-protection applications.

Material Properties

The accurate modeling of the overall thermally induced response of these materials requires the accurate modeling of all of the chemical and physical processes that occur over the temperature range of interest. The properties/modeling parameters for H41N and MXBE-350 are listed in Tables 2 and 3, respectively. In both tables, mass loss or temperature ranges are specified over which the modeling parameter or function is applicable. With the exception of permeability, porosity, and volumetric heat transfer coefficient data, all of the properties/parameters listed in Tables 2 and 3 were assembled from a study performed by Henderson and Wiecek.[5] Permeability and porosity data and corresponding parameters were taken from more recent studies by Ramamurthy[8] and Doherty,[9] respectively, whereas volumetric heat transfer coefficient data and corresponding parameters were taken from an experimental study performed by Florio et al.[7]

Results and Discussion

Using the appropriate equations and thermal property relations outlined earlier, the thermally induced responses of H41N and MXBE-350 were evaluated. For both materials, the model was exercised for a 0.03-m-thick slab with a pure radiation heat flux of 279.7 kW/m^2 applied to the front surface, $x = 0$. The back surface, $x = L$, was prescribed to be insulated. The initial temperature and pressure were taken as 40°C and 1.01325×10^5 Pa, respectively.

For H41N, the computer simulation run was made utilizing 151 nodes and a time step of 0.2 s. For MXBE-350, the computer simulation run was made utilizing 151 nodes and a time step of 0.004 s. For each material, it was determined that further reduction in the number of nodes or in the time step altered the results by less than 1%.

The thermally induced responses of H41N and MXBE-350, as a function of time and depth, are shown in Figs. 1-10 and 11-16, respectively. All profiles are shown at times of 100, 200, 400, 600, and 800 s.

Figure 1 illustrates the temperature history of the solid material for H41N. Evident from this figure are the steep temperature profiles, present primarily because of the low solid thermal conductivity. Also evident is the expansion of the material, as each successive time curve ends further be-

Table 1 Material composition

Constituent	% Composition (mass) H41N	% Composition (mass) MXBE-350
Resin		
Phenol-formaldehyde (phenolic)	39.5	28.0
Acrylonitrile-butadiene	—	14.0
Total resin content	39.5	42.0
Filler		
Glass fibers and talc	60.5	—
Glass fiber (mat)	—	43.0
Glass powder	—	15.0
Total filler content	60.5	58.0

Table 2 Material properties for H41N

Property/ parameter	Function[a]	Range[a]
ρ_v, kg/m^3	1810.0	
k_v, W/m-K	$0.80+2.76\times10^{-4}T$	$20\leq T\leq 1000$
k_c, W/m-K	$0.96+8.42\times10^{-4}T$ $-4.07\times10^{-6}T^2+5.32\times10^{-9}T^3$	$20\leq T\leq 1000$
C_{pv}, kJ/kg-K	$1.05+9.76\times10^{-4}T$	$20\leq T\leq 1200$
C_{pc}, kJ/kg-K	$0.88+7.60\times10^{-4}T$	$20\leq T\leq 1200$
ϕ_v (-)	0.113	
ϕ_c (-)	0.274	
δ (-)	-0.866	$m_s/m_o\leq 1$
γ_v, m^2	6.18×10^{-18}	
γ_c, m^2	4.85×10^{-15}	
Ψ_v, 1/K	0	
Ψ_c, 1/K	0	
ζ (-)	-2619.0	$0.795\leq m_s/m_o\leq 0.99$
c	0	
α_v, 1/K	8.59×10^{-5}	
α_c, 1/K	-7.42×10^{-5}	$0.492< m_s/m_o\leq 0.99$
	-5.93×10^{-4}	$m_s/m_o=0.492$
η, 1/K	8.03×10^{-4}	$0.92\leq m_s/m_o\leq 0.99$
	-1.68×10^{-4}	$0.81\leq m_s/m_o<0.92$
ξ (-)	0.967	$0.92\leq m_s/m_o\leq 0.99$
	0.445	$0.81\leq m_s/m_o<0.92$
	-2.19×10^{-2}	$0.492< m_s/m_o<0.795$
A, 1/s	1.98×10^{29}	$m_s/m_o\geq 0.91$
	8.17×10^{18}	$0.795\leq m_s/m_o>0.91$
	2.62×10^{7}	$m_s/m_o<0.795$
E, kJ/kmole	2.60×10^{5}	$m_s/m_o\geq 0.795$
	3.54×10^{5}	$m_s/m_o>0.795$
n (-)	17.33	$m_s/m_o\leq 0.91$
	6.30	$0.795\leq m_s/m_o<0.91$
	0.53	$m_s/m_o<0.795$
Q, kJ/kg	-234.0	$m_s/m_o\geq 0.795$
	-2093.0	$m_s/m_o<0.795$
ϵ_v	0.84	
ϵ_c	0.88	
a	2.22×10^{-6}	$m_s/m_o\leq 1$
b	0.703	$m_s/m_o\leq 1$

[a] Temperature in °C.

Table 3 Material properties for MXBE-350

Property/ parameter	Function[a]	Range[a]
ρ_v, kg/m^3	1720.0	
k_v, W/m-K	$0.64+1.14\times10^{-5}T$	$20\leq T\leq 1000$
k_c, W/m-K	$0.50+1.88\times10^{-3}T$ $-6.36\times10^{-6}T^2+6.74\times10^{-9}T^3$	$20\leq T\leq 1000$
C_{pv}, kJ/kg-K	$1.26+4.61\times10^{-4}T$	$20\leq T\leq 800$
C_{pc}, kJ/kg-K	$0.67+7.12\times10^{-4}T$	$20\leq T\leq 800$
ϕ_v (-)	0.124	
ϕ_c (-)	0.340	
δ (-)	-0.570	$m_s/m_o\leq 1$
γ_v, m^2	2.73×10^{-17}	
γ_c, m^2	1.82×10^{-13}	
Ψ_v, 1/K	0	
Ψ_c, 1/K	-10.50	$m_s/m_o\leq 0.99$
ζ (-)	-48380.3	$m_s/m_o\leq 0.99$
c	73.61	
α_v, 1/K	6.32×10^{-5}	
α_c, 1/K	-2.75×10^{-5}	
η, 1/K	-2.05×10^{-4}	$0.78\leq m_s/m_o\leq 0.99$
	1.35×10^{-4}	$0.71\leq m_s/m_o<0.78$
ξ (-)	0.384	$0.78\leq m_s/m_o\leq 0.99$
	5.67×10^{-2}	$0.71\leq m_s/m_o<0.78$
	6.04×10^{-2}	$0.505\leq m_s/m_o<0.70$
A, 1/s	2.48×10^{44}	$m_s/m_o\geq 0.96$
	8.47×10^{16}	$0.70\leq m_s/m_o<0.96$
	8.65×10^{6}	$m_s/m_o<0.70$
E, kJ/kmole	2.20×10^{5}	$m_s/m_o\geq 0.70$
	3.42×10^{5}	$m_s/m_o<0.70$
n (-)	50.64	$m_s/m_o\geq 0.96$
	4.20	$0.70\leq m_s/m_o<0.96$
	0.21	$m_s/m_o<0.70$
Q, kJ/kg	-553.0	$m_s/m_o\geq 0.70$
	-2093.0	$m_s/m_o<0.70$
ϵ_v	0.80	
ϵ_c	0.80	
a	1.71×10^{-6}	$m_s/m_o\leq 1$
b	0.783	$m_s/m_o\leq 1$

[a] Temperature in °C.

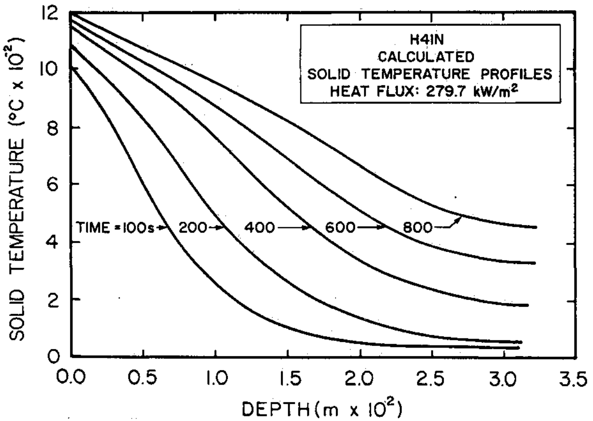

Fig. 1 Solid temperature profiles for H41N.

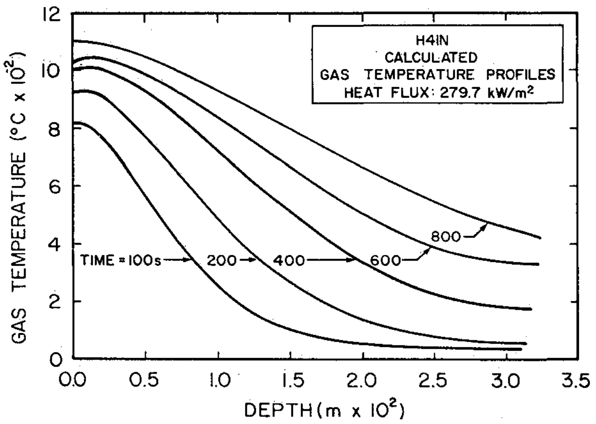

Fig. 2 Gas temperature profiles for H41N.

yond the previous one. By 800 s, the material has expanded from an initial thickness of 0.03 m to approximately 0.032 m.

Figure 2 illustrates the temperature history of the product gas for H41N. A comparison of Figs. 1 and 2 shows large differences between the two temperature profiles. In fact, deviations from local thermal equilibrium as high as 200°C are predicted. Note that for a particular time, the major deviation from thermal equilibrium occurs at the front surface. This is expected because this surface is exposed to the radiant heat flux, and thus subject to rapid heating. However, this deviation from thermal equilibrium decreases with increasing time due to the balancing of absorbed energy with emitted energy at the solid surface.

Figure 3 shows the mass-loss history for H41N. The ordinate axis represents the fraction of mass remaining $m_s/m_{s,o}$. For H41N, the pyrolysis reactions result in a mass loss of about 20%, i.e., $m_s/m_{s,o}=0.8$. A comparison of Figs. 1 and 3 shows that the pyrolysis reactions are initiated in the solid temperature range of approximately 350–375°C and reach completion in the solid temperature range of approximately 1000–1100°C. As a result, it is evident from Fig. 3 that the reactions have reached completion at the heated surface for times greater than 100 s, and by 800 s the reaction zone has progressed to the back surface. Also evident from this figure is that the radiant heat flux of 279.7 kW/m^2 does not supply sufficient incident energy for the initiation of the carbon-silica reactions in this material, which occur when $m_s/m_{so}<0.8$.

The dimensionless pressure p/p_o profiles for H41N are shown in Fig. 4. As can be seen, the peak pressure moves further into the material with increasing time, following the pyrolysis reaction zone. A comparison of Figs. 3 and 4 shows that for a given time the peak pressure takes place just after the onset of pyrolysis ($m_s/m_{s,o}>0.98$), primarily due to low material permeability and porosity in this region. The sole exception to this is at 800 s, where as discussed earlier the pyrolysis zone has progressed through the material. As a result, the material permeability at the back surface has become quite large by 800 s. Hence, the gas can flow quite freely out the back surface, resulting in a reduction in the entire pressure field.

Figure 5 shows the decomposition gas mass flux $\dot{m}''_g$ profiles in the material. A negative value on the ordinate axis indicates flow toward the heated surface, while a positive value indicates flow toward the back surface. As expected from the preceding discussion, the majority of the decomposition gas exits the material by way of the heated surface, except at 800 s where appreciable flow out the back surface occurs.

The ratio of the instantaneous decomposition gas mass storage to the initial gas mass occupying the pores, $m_g/m_{g,o}$, is depicted in Fig. 6. Comparison of Figs. 3 and 6 reveals that the peak gas storage occurs midway in the pyrolysis reaction region. Secondary plateaus are also seen in Fig. 6 within the virgin material, where no mass loss has occurred. These plateaus are created as a result of gas flow toward the back surface. This gas becomes trapped due to the low material permeability in this region.

The expansion profiles for H41N are shown in Fig. 7. The fractional length change $(\Delta x-\Delta x_o)/\Delta x_o$ is represented on the ordinate axis. Inspection of the figure clearly reveals the distinct stages of expansion described earlier. As can be seen, expansion as high as 15% occurs as a result of pyrolysis. Clearly, this is significant and has a direct impact on the overall response of the material. As with pressure, expansion follows the pyrolysis zone, moving further into the material with increasing time. However, examination of Figs. 4 and 7 shows that the peak expansion lags the peak pressure for a given time. The peak expansion actually occurs midway in the pyrolysis region. This is thought to occur because the char material in the pyrolysis region has a much lower specific strength than the virgin material. Hence, the char structure is weaker, allowing for more expansion as a result of internal pressurization. A more detailed discussion of the expansion characteristics of these materials is presented elsewhere.[10]

Figure 8 illustrates volumetric heat transfer coefficient h_v profiles between decomposition gases and the solid within the pore network of the H41N. As expected from Eq. (13), the peak value of h_v for a given time occurs where the pressure gradient is steepest. Comparison of Figs. 8 and 4 shows that there is a sharp change in the volumetric heat transfer coefficient profile corresponding to the occurrence of the peak pressure. This phenomenon does not occur at 800 s because the pressure profile is much flatter than at the earlier time. However, at 800 s, h_v approaches zero at a depth of about 2.2 cm because of a zero pressure gradient at this location.

Figure 9 illustrates the temperature history of the solid material for MXBE-350. A comparison of Figs. 1 and 9 shows

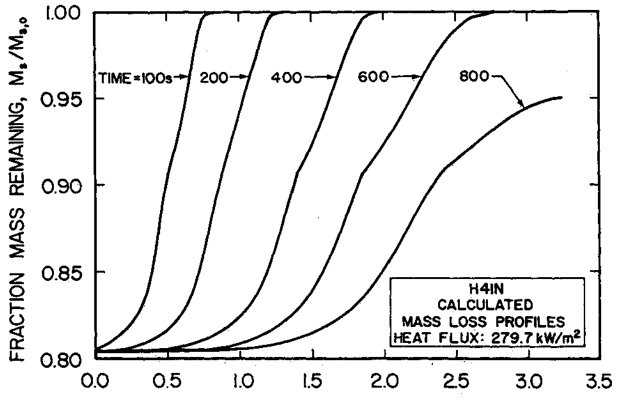

Fig. 3 Mass-loss profiles for H41N.

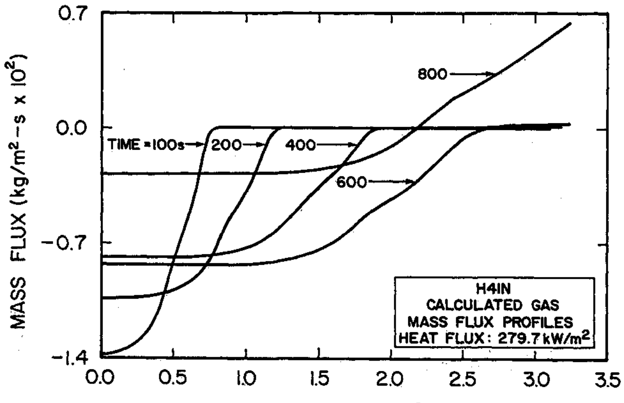

Fig. 5 Gas mass flux profiles for H41N.

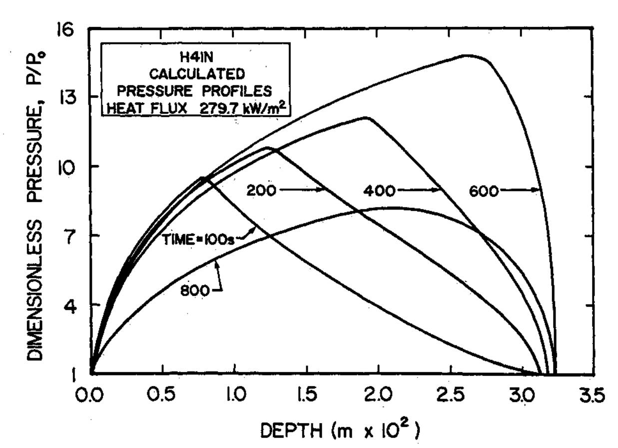

Fig. 4 Pressure profiles for H41N.

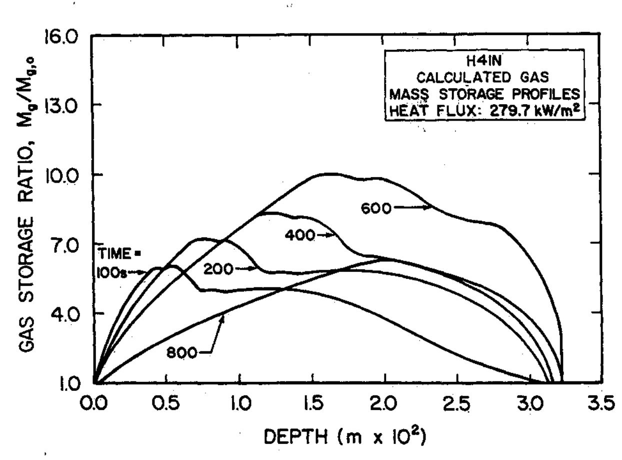

Fig. 6 Gas mass storage profiles for H41N.

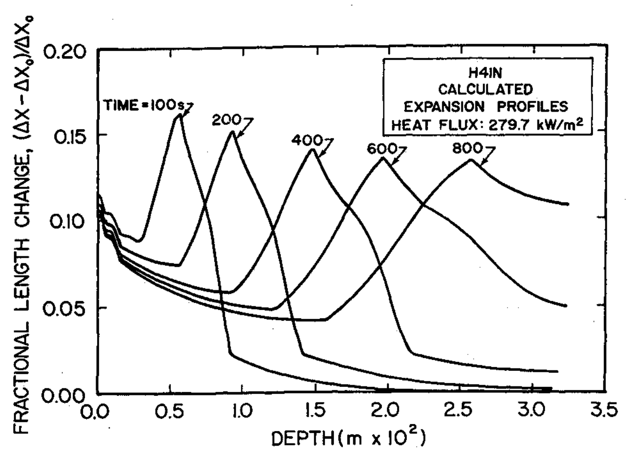

Fig. 7 Expansion profiles for H41N.

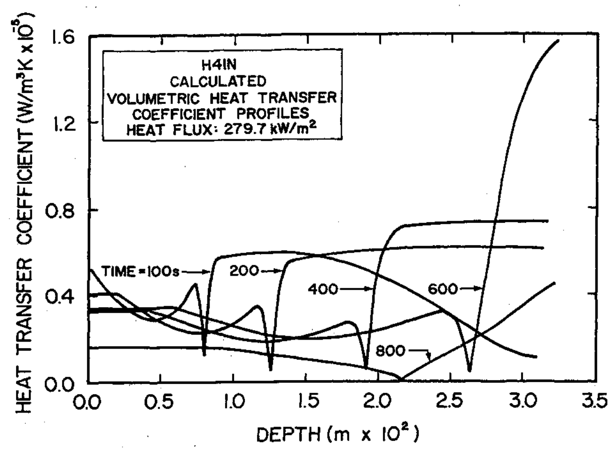

Fig. 8 Volumetric heat transfer coefficient profiles for H41N.

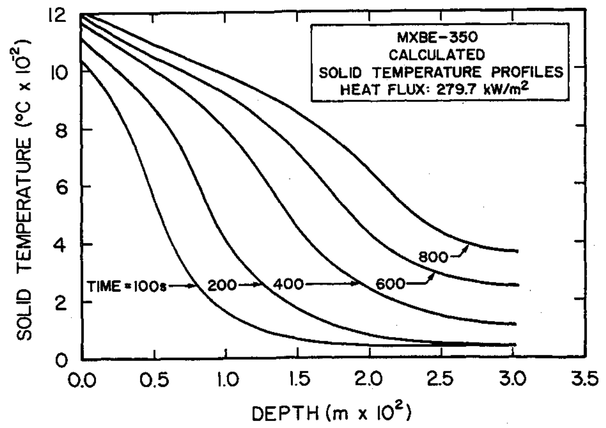

Fig. 9 Solid temperature profiles for MXBE-350.

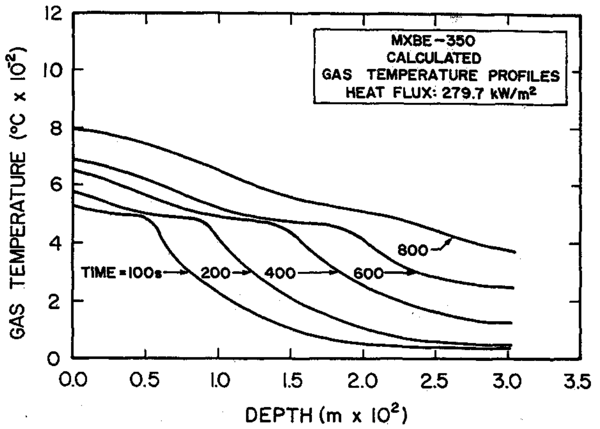

Fig. 10 Gas temperature profiles for MXBE-350.

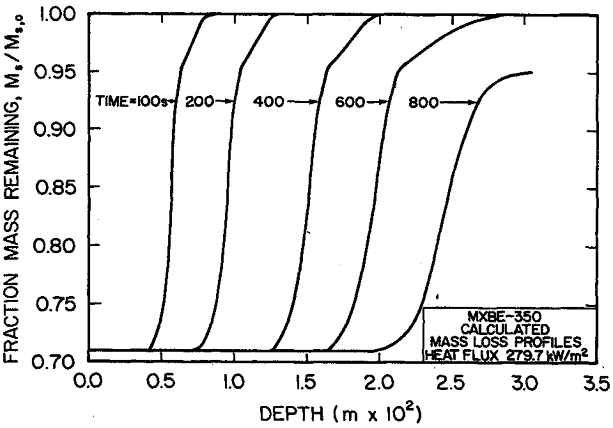

Fig. 11 Mass-loss profiles for MXBE-350.

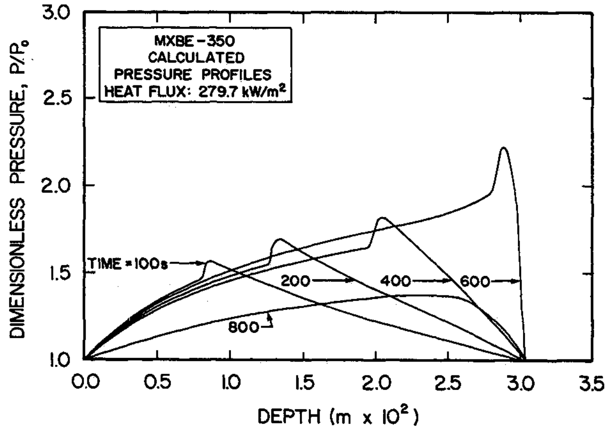

Fig. 12 Pressure profiles for MXBE-350.

that while the thermal response of H41N and MXBE-350 are quite similar, the temperature gradients for MXBE-350 are greater for a given temperature. This is primarily due to the lower thermal conductivity of both the virgin and char components of MXBE-350 at a given temperature, which is a result of its rubber-modified resin system.

The product gas temperature history for MXBE-350 is shown in Fig. 10. A comparison of Figs. 9 and 10 reveals differences as high as 500°C existing between the two profiles at the front surface. In contrast, deviations from local thermal equilibrium as high as 200°C were seen for H41N. This difference is a result of lower volumetric heat transfer coefficients in MXBE-350.[7] Lastly, the history of the gas temperature profiles for MXBE-350 is similar to that discussed for the gas temperature profiles for H41N.

Figure 11 illustrates the mass-loss history of MXBE-350. A comparison of Figs. 9 and 11 reveals that the pyrolysis reactions begin in the solid temperature range of approximately 250–300°C and reach completion in the range of approximately 700–750°C. Hence, the pyrolysis reactions in MXBE-350 result in a solid mass loss of approximately 30% and cover a solid temperature range of about 500°C. In contrast, the pyrolysis reactions in H41N occur over a temperature range of about 750°C and produce a solid mass loss of approximately 20%. This difference in kinetic behavior is thought to be due to the addition of acrylonitrile-butadiene to the basic phenolic system of MXBE-350.

Figure 12 depicts the dimensionless pressure profiles for MXBE-350. As with H41N, the pressure peaks during the initial stages of decomposition as a result of the low permeability and porosity in the region. Also, similar pressure-time behavior is seen in the two materials and was discussed for H41N. However, a direct comparison of Figs. 4 and 12 reveals that both the shape and magnitude of the pressure profiles in the two materials are vastly different. The peak value of p/p_o for MXBE-350 is approximately 2.25 at 600 s, as compared to about 13 for H41N. This is best explained by the fact that MXBE-350 has a permeability of approximately two orders of magnitude greater than that of H41N for the entire temperature range of this study, allowing for gas to flow more easily out of the pore network. The high permeability of MXBE-350 most likely occurs because of the continuous-strand glass mat used in the manufacturing of the material. MXBE-350 also has much steeper pressure gradients in the pyrolysis zone prior to the peak value of p/p_o. This steep profile is a result of high permeability and porosity gradients caused by rapid solid mass decomposition. A comparison of Figs. 3 and 11 reveals much steeper mass-loss profiles in MXBE-350, confirming a more rapid rate of decomposition. This is also confirmed by the fact that MXBE-350 loses 10% more mass than H41N during pyrolysis over a much smaller temperature range.

The fractional length change profiles for MXBE-350 are depicted in Fig. 13. A comparison of Figs. 7 and 13 shows that the general expansion behavior of MXBE-350 and H41N is similar. However, the magnitude of the expansion for MXBE-350 is seen to be considerably less than that of H41N. This is best explained by the lower internal pressures observed in MXBE-350. The relationship between internal pressurization and expansion was discussed earlier. As with H41N, the material expansion lags the pressure. The explanation of this phenomenon is the same as stated earlier for H41N.

Volumetric heat transfer coefficient h_v profiles for MXBE-350 are shown in Fig. 14. A comparison of Figs. 8 and 14 reveals similar profiles in both materials. However, the values of h_v for MXBE-350 are about one order of magnitude lower than those of H41N. This difference in magnitude explains why larger deviations from local thermal equilibrium exist in MXBE-350. The reason for the smaller values of h_v in MXBE-350 is the fact that MXBE-350 has a pore surface area roughly six to seven times less than that of H41N. Also, MXBE-350 has a much higher permeability, causing shorter contact time between the two phases locally, and hence limiting energy transfer. A more detailed discussion on the measurement and modeling of h_v in these materials is presented in great detail elsewhere.[7]

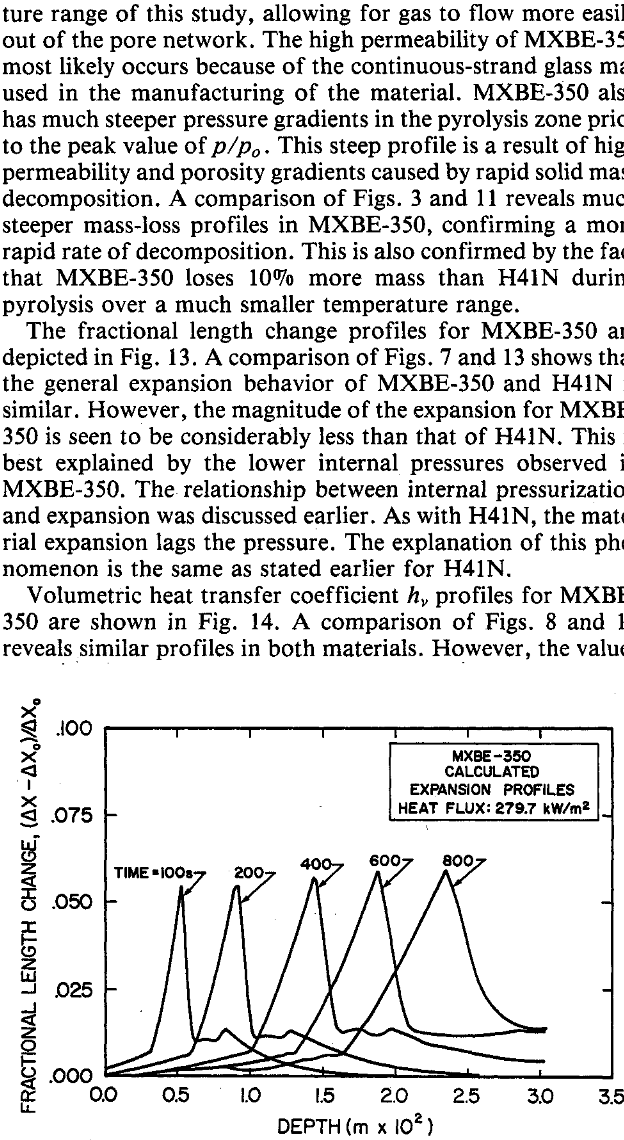

Fig. 13 Expansion profiles for MXBE-350.

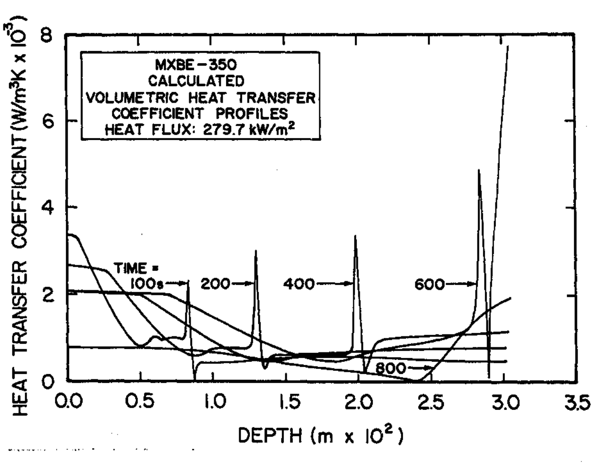

Fig. 14 Volumetric heat transfer coefficient profiles for MXBE-350.

The accuracy of the model was established by comparing predicted and experimental solid temperature and gas pressure profiles for H41N. The experimental temperature and pressure profiles were obtained from a study performed by Ramamurthy[8] for the same initial- and boundary-value conditions and sample geometry as were used in the numerical scheme.

Ramamurthy implanted thermocouples in the material at known initial depths in order to record solid temperature data. The measurement of internal gas pressure was performed by inserting hypodermic tubing into the material, and sealing the tube in with a ceramic cement so gas could not escape. A miniature strain gauge was fixed on the free end of each tube, and the pressure which developed in the material during decomposition was recorded as a voltage corresponding to a deflection of the strain gauge. Voltage/pressure relations were

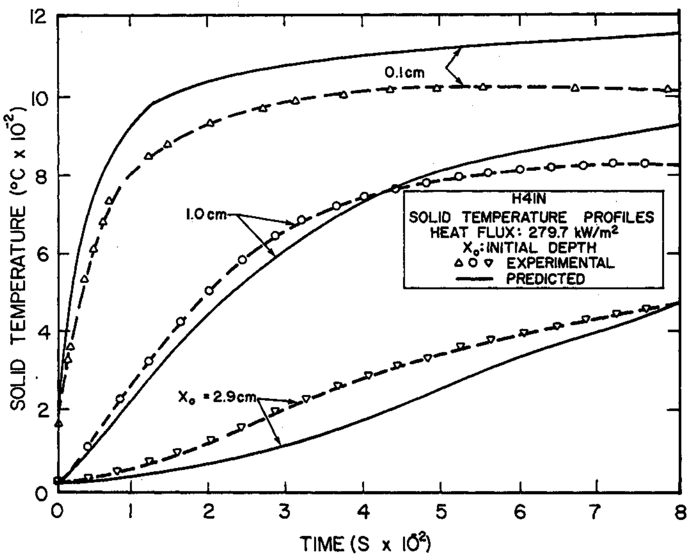

Fig. 15 Comparison of predicted and experimental solid temperature profiles for H41N.

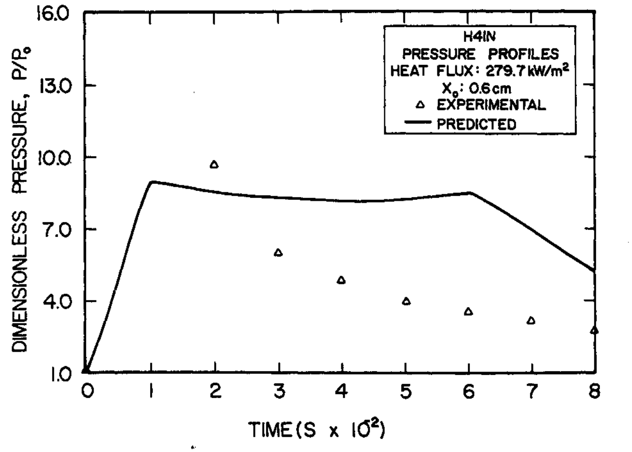

Fig. 16 Comparison of predicted and experimental pressure profile at 0.6 cm for H41N.

supplied by the strain-gauge manufacturer. For H41N, solid temperature and gas pressure readings were taken in the same sample.

Figure 15 shows a comparison of analytical and experimental solid temperature profiles as a function of time for initial depths of 0.1, 1.0, and 2.9 cm. Evident from this figure is the relatively good agreement between analysis and experiment.

Analytical and experimental gas pressure profiles are compared in Fig. 16 as a function of time for a depth of 0.6 cm. There appears to be excellent agreement between the peak analytical and experimental pressures, with peaks of 9 and 9.7 atm, respectively. However, the experimental pressure drops off very rapidly after the peak value. Ramamurthy attributes this behavior to poor cement bonding between the hypodermic tubing and the specimen, magnified by differences in the expansion characteristics of the cement and specimen. Consequently, cracks develop at the interface resulting in leakage of gas. Ramamurthy concludes that as a result of experimental difficulties, the internal gas pressure is at least as high at the recorded pressure.

Concluding Remarks

The newly developed numerical model presented in this study predicts the thermally induced response of decomposing, glass-filled polymer composites without the idealized assumption of the existence of local thermal equilibrium. The thermal response of two composites has been quantified for a given set of boundary conditions. It has been demonstrated that polymer composites exhibit complex thermally induced behavior when heated to high temperatures. Also demonstrated is the fact that even seemingly small differences in materials and their method of preparation have a dramatic effect upon predicted thermal behavior.

The results of this study also indicate that local thermal equilibrium does not exist in either material. In fact, in MXBE-350, solid-to-product gas temperature differences of as high as 500°C were predicted to exist locally during decomposition, whereas for the tighter, more fibrous H41N differences of only as high as 200°C were predicted. A preliminary investigation into the effect of the assumption of local thermal equilibrium reveals significant differences in the predicted overall response when the assumption is used. As expected, predicted decomposition for the idealized case lags that of the actual case. A more detailed discussion on the effect of the assumption of local thermal equilibrium on the overall thermally induced response of these materials will be presented in papers to follow.

Acknowledgments

The authors wish to acknowledge the financial support of the U.S. Army Research Office, Metallurgy and Materials Science Division, under Grants DAA629-84-K-0912 and DAAL03-86-G-0072.

References

[1] Kung, H. C., "A Mathematical Model of Wood Pyrolysis," *Combustion and Flame,* Vol. 18, 1972, pp. 185–195.

[2] Kansa, E. J., Perlee, H. E., and Chaiken, R. F., "Mathematical Model of Wood Pyrolysis Including Internal Forced Convection," *Combustion and Flame,* Vol. 29, 1977, pp. 311–324.

[3] Anderson, C. E., Jr., and Wauters, D. K., "A Thermodynamic Heat-Transfer Model for Intumescent Systems," *International Journal of Engineering Science,* Vol. 22, No. 7, 1984, pp. 881–889.

[4] Henderson, J. B., Wiebelt, J. A., and Tant, M. R., "A Model for the Thermal Response of Polymer Composite Materials with Experimental Verification," *Journal of Composite Materials,* Vol. 19, 1985, pp. 579–595.

[5] Henderson, J. B., and Wiecek, T. E., "A Numerical Study of Thermally Induced Response of Decomposing, Expanding Polymer Composites," *Warme- und Stoffubertragung,* Vol. 22, 1988, pp. 275–284.

[6] Ladacki, M., "Silicon Carbide in Ablative Chars," *AIAA Journal,* Vol. 4, No. 8, 1966, pp. 1445–1447.

[7] Florio, J., Jr., Henderson, J. B., and Test, F. L., "Experimental Determination of Volumetric Heat-Transfer Coefficients in Decomposing Polymer Composites," American Society of Mechanical Engineers, New York, ASME Paper, Dec. 1989.

[8] Ramamurthy, H., "An Experimental Investigation into the Thermophysical Properties of Decomposing Polymer Composites," M.S. Thesis, Univ. of Rhode Island, Kingston, RI, 1988.

[9] Doherty, M. P., "Characterization of the Porous Microstructure of Decomposing Glass-Filled Polymer Composites," M.S. Thesis, Univ. of Rhode Island, Kingston, RI, 1988.

[10] Florio, J., Jr., Henderson, J. B., and Test, F. L., "Measurement of the Thermochemical Expansion of Porous Composite Materials," *High Temperatures-High Pressures,* Vol. 21, 1989, pp. 157–165.